




Van Hove singularity, flat band, and phonon-mediated superconductivity in topological perovskite carbides

Yunqun Li , Mingmin Zhong *, Meng Ju, Yu-Hao Wei, and Min-Quan Kuang †

Chongqing Key Laboratory of Micro & Nano Structure Optoelectronics, and School of Physical Science and Technology, Southwest University, Chongqing 400715, People's Republic of China



(Received 26 April 2024; revised 26 June 2024; accepted 15 August 2024; published 27 August 2024)

Recently, the emergence of van Hove singularity, flat band, and Dirac cone in kagome materials has attracted tremendous interest as they are closely related to the superconductivity. Here, based on first-principles calculations, we propose these features can be realized in the topological perovskites $ACPd_3$ ($A = \text{Mg, Ca, Sr}$). In particular, the Dirac point is observed near the Fermi level with the spin-orbit coupling. The superconducting transition temperature T_c is estimated to be 19.05, 15.37, and 10.25 K for $MgCPd_3$, $CaCPd_3$, and $SrCPd_3$ by solving the Allen-Dynes modified McMillan formula, respectively. In general, the high T_c can be attributed to the large electronic density of states near the Fermi level, which arises from the van Hove singularity and flat band. Noticeably, the declining trend of T_c from $MgCPd_3$ to $SrCPd_3$ can be ascribed to the decreasing electron-phonon coupling that is related to the weakening of electron correlation. This point is further verified by doping holes (electrons) in $CaCPd_3$, i.e., the T_c would gradually increase to 18.41 K when the flat band gets more and more dispersionless. Thus these perovskites provide solid platforms to explore the interplay among band topology, electron correlation and superconductivity.

DOI: [10.1103/PhysRevB.110.064519](https://doi.org/10.1103/PhysRevB.110.064519)

I. INTRODUCTION

Recently, kagome materials with corner-sharing triangles have attracted much interest due to their unique properties in band topology, magnetism, superconductivity, and novel electronic orders, which arise from the interplay among geometry, spin and correlation [1–8]. Especially, the emergent Dirac point (DP), van Hove singularity (VHS) and flat band (FB) in kagome materials have also been reported in twisted angle graphene [9–12], cuprate superconductors [13–16] and iron-based superconductors [17–19]. Since the DP embodies topology, flat band indicates correlation effect, and the VHS can lead to electronic instability towards exotic orders, these features might be the typical electronic structures to obtain unconventional superconductors [10,20] and even topological superconductors [11]. Then, one may ask whether there are other scenarios to realize the DP, VHS, FB and superconductivity in a specific material. Here, we propose the above features can be realized in perovskite carbides $ACPd_3$ ($A = \text{Mg, Ca, Sr}$).

Actually, perovskites are one of the well-known ternary compounds, which have lots of interesting properties, such as superconductivity [21], non-Fermi liquid behavior [22–24], strong electron-electron correlation [25], etc. He *et al.* reported very interesting and atypical superconductivity of $MgCNi_3$ perovskite, with the critical temperature $T_c = 8$ K [26]. The large amount of nickel atoms usually results in magnetism rather than superconductivity. Hence, extensive

research has been carried out to explore the exact nature of the superconducting state and its microscopic origin. However, the existing measurements on NMR, specific heat, penetration depth, critical field, critical current, superfluid density, and tunneling spectroscopy reveal that the pairing mechanism of $MgCNi_3$ is still controversial. Some experiments suggest that $MgCNi_3$ is a conventional superconductor with s -wave pairing [27–33], while others indicate that $MgCNi_3$ has an unconventional pairing state [34–37]. Thus designing isostructural superconductors would be helpful to explore the underlying pairing mechanism of $MgCNi_3$. Other related materials, such as carbide [38–40], boride [41–43], nitride [44–48], and oxide perovskites (or antiperovskites) [43,49–51], have been proved experimentally to be superconductors in the following years. Besides, combining with interpretable machine learning, dozens of perovskite (antiperovskite) materials are identified as superconductors by electron-phonon calculations [52]. Although these researches reported the superconducting properties [the T_c , electron-phonon coupling (EPC) and so on] of perovskite (antiperovskite) materials, rare studies are focus on the topological properties and the trend of superconductivity varying with element compositions.

To realize the DP, VHS, and FB in perovskite (antiperovskite) compounds, and explore the variation tendency of superconductivity, we report three nonmagnetic perovskite superconductors, namely, $ACPd_3$ ($A = \text{Mg, Ca, Sr}$) by first-principles calculations. $CaCPd_3$ has been synthesized in experiment and the other two perovskites are derived from elemental substitution. Here, the stability is also checked from thermodynamics, mechanics and dynamics by calculating the formation energy, elastic constants and phonon spectra, respectively. When the spin-orbit coupling (SOC) effect is

*Contact author: zhongmm@swu.edu.cn

†Contact author: mqkuang@swu.edu.cn

ignored, the VHS, FB, and triple point (TP) appear near the Fermi level. When the SOC is turned on, the TP is gapped and transformed to DP. The corresponding irreducible representations (IRs) and relative topological surface states for the TP and DP demonstrate that they are nontrivial topological metals. The obtained high superconducting critical temperatures ($T_c = 19.05, 15.37, \text{ and } 10.25 \text{ K}$ for MgCPd_3 , CaCPd_3 , and SrCPd_3 , respectively) can attribute to the strong electron-phonon coupling (EPC) that is closely related to the VHS and FB near the Fermi level. This point is further verified in the variation trend of superconducting temperature by doping electrons (holes) in CaCPd_3 . Moreover, the coexistence of superconductivity and topological surface states (TSS) near the Fermi level provides promising platforms for the search of topological superconductors.

II. COMPUTATION METHODS

The first-principles calculations with the framework of density functional theory (DFT) are performed by using the QUANTUM ESPRESSO package [53]. The Perdew-Burke-Ernzerhof (PBE) parameterized generalized gradient approximation (GGA) is chosen to describe the exchange-correlation energy [54]. The projector-augmented-wave (PAW) pseudopotential [55] is utilized to model the interaction between electrons and ionic cores. The kinetic energy cutoff for wave functions (charge density and potential) is set 90 (360) Ry. The total energy tolerance and residual force on each atom are less than 10^{-8} Ry and 10^{-7} Ry/bohr in the structure optimization. The Brillouin zone (BZ) is sampled on a $12 \times 12 \times 12$ Monkhorst-Pack k -point grid for the self-consistent calculations. A denser grid $24 \times 24 \times 24$ k -point grid is used to obtain the density of states and band structures. Phonon dispersion curves of the normal states are calculated based on density functional perturbation theory [56], where a $6 \times 6 \times 6$ q -point grid is adopted for the electron-phonon coupling calculations. The phonon-related calculations are carried out without including the SOC effect, because it is less important in describing the vibrational properties [57]. The Fermi velocity projected on the Fermi surfaces is drawn by using FERMISURFER code [58]. The nontrivial topology properties are calculated by the iterative Green's function as provided in the WANNIERTOOLS package [59,60], where a tight-binding method based on the maximally localized Wannier function (MLWF) is employed [61,62]. The mechanic properties are calculated by the strain-stress method as implemented within the Vienna *ab initio* simulation package (VASP) [63].

In the EPC calculations, the mode-resolved EPC λ_{qv} is calculated according to the Migdal-Eliashberg theory, by

$$\lambda_{qv} = \frac{\gamma_{qv}}{\pi h N(E_F) \omega_{qv}^2}, \quad (1)$$

where $N(E_F)$ is the electronic DOS at Fermi level, ω_{qv} refers to the phonon frequency, and γ_{qv} is the phonon linewidth estimated by

$$\gamma_{qv} = \frac{2\pi \omega_{qv}}{\Omega_{\text{BZ}}} \sum_{k,n,m} |g_{kn,k+qm}^v|^2 \delta(\varepsilon_{kn} - \varepsilon_F) \delta(\varepsilon_{k+qm} - \varepsilon_F), \quad (2)$$

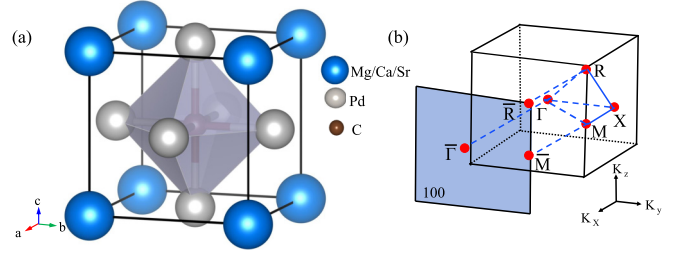


FIG. 1. (a) The crystal structure of ACPd_3 ($A = \text{Mg, Ca, Sr}$). (b) The corresponding Brillouin zone (BZ) with high symmetry points and the projected (100) surface.

where Ω_{BZ} is the volume of the BZ, ε_{kn} and ε_{k+qm} denote the Kohn-Sham eigenvalues, and $g_{k,n,k+qm}^v$ represents the EPC matrix element. The $g_{k,n,k+qm}^v$ can be determined self-consistently by linear response theory [64]. The Eliashberg electron-phonon spectral function $\alpha^2 F(\omega)$ is obtained based on the Eliashberg equation:

$$\alpha^2 F(\omega) = \frac{1}{2\pi N(E_F)} \sum_{qv} \frac{\gamma_{qv}}{\omega_{qv}} \delta(\omega - \omega_{qv}). \quad (3)$$

The electron-phonon mass enhancement parameter λ can be obtained directly from the integration of the λ_{qv} in the first Brillouin zone for all phonon modes or defined as the first reciprocal momentum of the spectral function:

$$\lambda(\omega) = \sum_{qv} \lambda_{qv} = 2 \int_0^\omega \frac{\alpha^2 F(\omega')}{\omega'} d\omega', \quad (4)$$

and the logarithmic average frequency ω_{log} is calculated by

$$\omega_{\text{log}} = \exp \left[\frac{2}{\lambda} \int_0^\infty \frac{d\omega}{\omega} \alpha^2 F(\omega) \log \omega \right]. \quad (5)$$

Based on the BCS theory [65] and the above results, the superconducting transition temperature T_c can be calculated by using the McMillian-Allen-Dynes formula:

$$T_c = \frac{\omega_{\text{log}}}{1.2} \exp \left[-\frac{1.04(1 + \lambda)}{\lambda - \mu^*(1 + 0.62\lambda)} \right], \quad (6)$$

where μ^* is the effective screened Coulomb repulsion constant and can be set at a typical value of 0.1.

III. RESULTS AND DISCUSSIONS

A. Crystal structure and stability

CaCPd_3 was synthesized by arc-melting and subsequent annealing at 700°C [66]. It crystallizes in a cubic perovskite structure with the space group $Pm\bar{3}m$ (No. 221). As shown in Fig. 1, the Ca atoms are at the center of the cubes located in Wyckoff position 1a (0.0, 0.0, 0.0), the C atoms are at the center of octahedra located in Wyckoff position 1b (0.5, 0.5, 0.5), and the Pd atoms are at the vertices of octahedra located in Wyckoff position 3c (0.0, 0.5, 0.5). The optimized lattice constant of CaCPd_3 is $a = 4.22 \text{ \AA}$ (Table S1), which is slightly larger than the experimental data of $a = 4.14 \text{ \AA}$ [66]. This overestimation is typical from the implementation of PBE functional. Then, we adopt the structure of CaCPd_3 as the parent structure, and replace Ca atoms by Mg and Sr,

respectively. As tabulated in Table S1, the optimized lattice parameter increases with the increase in the alkaline-earth metal atomic number.

Since the structural stability is the foundation of subsequent studies, calculations have been carried out to test the thermodynamic, mechanic, and dynamic stability of ACPd₃ ($A = \text{Mg, Ca, Sr}$). To ascertain the thermodynamic stability of this system, we first calculate the formation energy, defined as

$$E_{\text{form}} = \frac{E_{\text{tot}} - E_A - 3E_{\text{Pd}} - E_C}{5}, \quad (7)$$

in which E_{tot} denotes the total energy of perovskite ACPd₃ ($A = \text{Mg, Ca, Sr}$) in the conventional unit cell, $E_{A/\text{Pd}}$ is the energy of one Mg/Ca/Sr/Pd atom in face-centered cubic crystal phase, E_C is the energy of one C atom in hexagonal close-packed crystal phase. As shown in the last column of Table S1, the formation energies for these three perovskites are all negative, strongly demonstrating their thermodynamic stability. In addition, the mechanical stability is estimated by calculating the three independent elastic constants for the cubic phase, namely, C_{11} , C_{12} , and C_{44} . As reported in Table S1, the three independent elastic constants all fulfill the Born mechanically stable criteria: $C_{11} - C_{12} > 0$, $C_{11} + 2C_{12} > 0$, $C_{44} > 0$, indicating that these compounds are mechanically stable. Finally, the dynamical stability of all proposed structures is checked by calculating the phonon dispersion. As shown in Sec. III C, the absence of phonon modes with imaginary frequencies is an indication that these three perovskite structures are dynamically stable (Fig. 5). It is worth pointing out that the magnetic moments of ACPd₃ ($A = \text{Mg, Ca, Sr}$) are calculated by using the method of non-linear magnetic moment calculations [67]. The results show that all the magnetic moments in different cases are zero and these materials are treated as nonmagnetic systems in this work.

B. Electronic and topological properties

The band structures along the selected routes [see Fig. 1(b)] without considering the SOC effect are displayed in Fig. 2 (see also Fig. S1 in Ref. [68]). The highlighted color bands α , β , and γ cross the Fermi level, suggesting all these materials are metallic. In particular, only two bands cross the Fermi level for MgCPd₃ [Fig. 2(a)], and three bands cross the Fermi level for CaCPd₃ [Fig. 2(b)] and SrCPd₃ [Fig. 2(c)]. As shown in Fig. 2, the d electrons of Pd atoms dominate the bands around the Fermi level and play a prominent role in their metallic properties, while the s orbitals of Pd atoms and p orbitals of C atoms have a little contribution, and the contribution of alkaline-earth atoms is negligible (see also the orbital resolved band structures in Figs. S2 and S3 [68]).

Moreover, there are several important features in the band structures. First, the VHS is detected at the X point near the Fermi level. The presence of VHS can drive some novel physical phenomena, such as superconductivity [11,14,17,19,69] and Fermi surface instability [13,70–72]. This VHS moves down with the mass of alkaline-earth metal atoms increasing, and it just locates at the Fermi level for CaCPd₃. These VHSs stem from the hybridization of Pd- d and C- p orbitals (see the

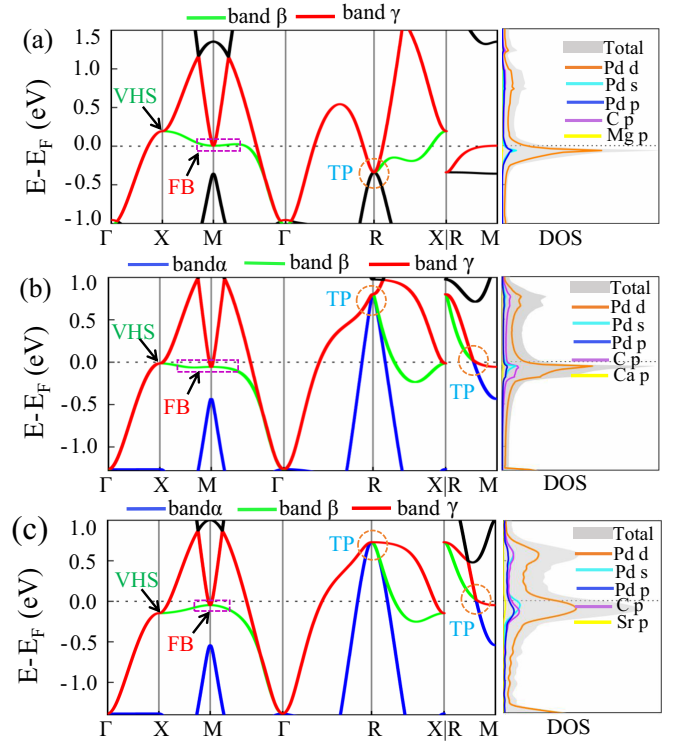


FIG. 2. The electronic band structures (left) and the partial density of states (DOSs) (right) without considering the SOC effect for (a) MgCPd₃, (b) CaCPd₃, and (c) SrCPd₃. The colored lines indicate the bands crossing the Fermi level. The van Hove singularities, flat bands and TPs are illustrated by the black arrows, purple rectangles, and orange circles, respectively.

projections in Figs. S2 and S3 [68]). The second remarkable feature is that there is a dispersionless flat band near the Fermi level along the path of X - M - Γ , which gives rise to the large electronic DOSs near the Fermi level (see the right panels of Fig. 2). These flat bands come from the mixture of Pd- s and Pd- d orbitals (see Figs. S2 and S3 [68]). Thirdly, the triple points with a threefold band degeneracy are observed in the electronic band, and highlighted in the orange circles. For MgCPd₃, the TP locates below the Fermi level (about -0.34 eV) at the high-symmetry point R . The TPs at R are far above the Fermi level about 0.80 eV for CaCPd₃ and 0.78 eV for SrCPd₃. It is worth noting that there is an accidental TP nearly locating at the Fermi level along the high-symmetry line R - M for CaCPd₃ and SrCPd₃. The hybridization of the p orbitals of alkaline-earth atoms and the Pd- $s/p/d$ orbitals dominates the TPs (see Figs. S2 and S3 [68]).

To further confirm the nontrivial topological nature of these TPs, the calculations of irreducible representations (IRs) [73] for the related bands are performed. The TP at R point for MgCPd₃ is a triply degenerate point with R_3^+ IR, and TPs at R for CaCPd₃ and SrCPd₃ with R_4^- and R_5^+ IRs, respectively (see Fig. S4 [68]). The corresponding surface states for CaCPd₃ is not clear, and covered by band states [see Fig. S4(d) [68]]. Due to far away from the Fermi level and unclear surface states, the TPs at R for CaCPd₃ and SrCPd₃ will not be further discussed. The TP along the direction

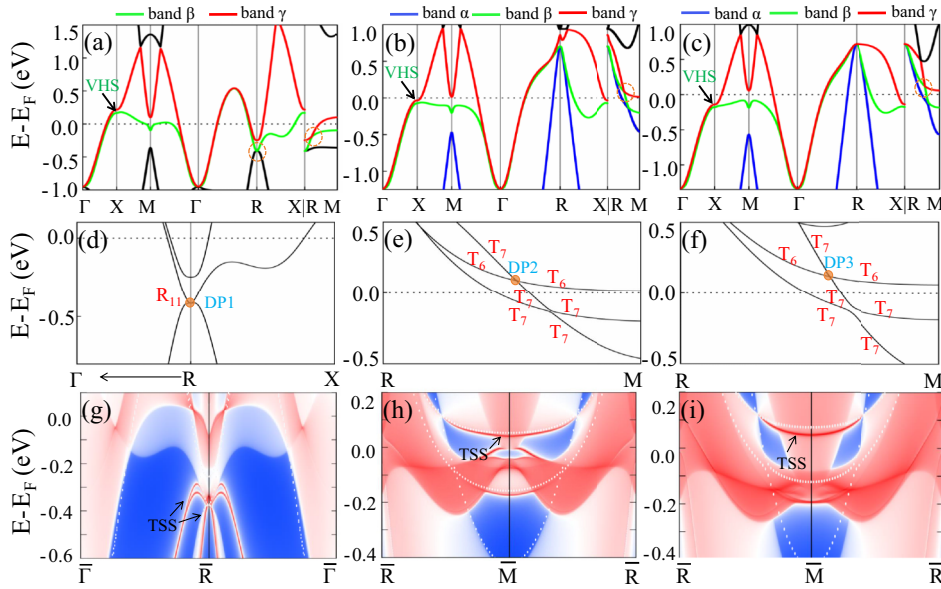


FIG. 3. The computed band structures including the SOC effect for (a) MgCPd₃, (b) CaCPd₃, and (c) SrCPd₃, where the VHSs and TPs are indicated by the black arrows and dashed orange circles, respectively. The enlarged views for the TPs and the corresponding IRs are displayed in (d) for MgCPd₃, (e) for CaCPd₃, and (f) for SrCPd₃, respectively. Besides, the calculated TSS of the TPs for (g) MgCPd₃, (h) CaCPd₃, and (i) SrCPd₃ on the (100) surface are also illustrated.

R - M is formed by the touching of nondegenerate band T_1 and a doubly degenerate band T_5 for CaCPd₃ and SrCPd₃ (see Fig. S4 [68]). Upon SOC inclusion, the electronic band structures near the Fermi level are modified a little due to strong SOC effect of Pd element (Fig. 3). One can see that the VHSs are robust at the X point for these three perovskites [Figs. 3(a)–3(c)]. Intriguingly, the above TPs transform into the fourfold degenerate Dirac points. For MgCPd₃, the DP1 at the time-reversal invariant momenta (TRIM) point R is an essential crossing point with a fourfold degenerate R_{11} IR [74] [Fig. 4(d)]. As for CaCPd₃ and SrCPd₃, the fourfold degenerate Dirac point DP2 and DP3 formed by two bands with different doubly degenerate IRs T_6 and T_7 , which are accidental crossing points along the R - M direction [74]. Moreover, the corresponding nontrivial TSSs for the case with and without SOC are clearly shown in Figs. 3 and S4, which are very close to the Fermi level and might be observed by the angle-resolved photoemission spectroscopy (ARPES) experiments. Besides, the crossing point along the R - M line in Fig. 3(a) is a DP. The calculation of IRs for the related bands indicates that there is a fourfold degenerate DP formed by two bands with different doubly degenerate IRs T_6 and T_7 . Unfortunately, the surface states are unclear and covered by the bulk states (Fig. S5 [68]).

In addition, the distributions of three-dimensional (3D) Fermi surfaces (FSs) (Fig. 4) and the orbital resolved two-dimensional (2D) FSs in the (110) plane (Fig. S6 [68]) echo the electronic band structures in Figs. 2, S2 [68], and S3 [68]. To be specific, the flat bands with localized electrons have a small Fermi velocity while these steep bands crossing Fermi level have a higher value. As for ACPd₃ ($A = \text{Mg, Ca, Sr}$), one can find both the holelike (constituted by bands α and β) and electron-like pockets (constructed by γ band) in the first BZ, which supply a potential platform to investigate the

superconducting pairing mechanism between multiple Fermi pockets [18,75–83].

C. Phononic and superconducting properties

These remarkable electronic features of ACPd₃ (the VHS, FB, and multiple Fermi pockets) inspire us to further explore their phonon vibrations, EPC, and phonon-mediated superconducting properties. We firstly project the weights of different atomic vibration modes on the phonon dispersion curves and then calculate the phonon density of states (PhDOS) (in Fig. 5). As shown in Figs. 5(a), 5(e), and 5(i), all the three acoustic branches and nine optical branches with low frequency are mostly contributed by alkaline-earth metal atoms and Pd atoms. The left three high-frequency optical branches, which are almost 20 meV away from the twelve low frequency branches, totally stem from the vibrations of light C atoms.

Specially, for MgCPd₃, the vibrations of the C atoms are mostly located in the high-frequency region (51–76 meV). The phonon vibrations of C atoms in different directions are coupled in this region. Noticeably, some vibrations of C atoms in the z direction spread to the low-frequency region, coupling with the vibrations of Pd atoms. The vibrations of Mg atoms are located in the narrow intermediate-frequency region (23–25 meV). The out-of-plane vibration modes of Mg atoms form a very flat band, which is responsible for a sharp peak in the PhDOS [Fig. 5(c)]. For CaCPd₃, vibrations of C, Ca, and Pd atoms almost separate from each other. The phonon vibrations of C atoms in different directions are coupled in the high-frequency region (49–70 meV). There is a flat phononic band in the intermediate frequency at 27 meV, which comes from the Ca _{z} vibrations. For SrCPd₃, the out-of-plane vibration modes of Pd atoms contribute to a flat band in the

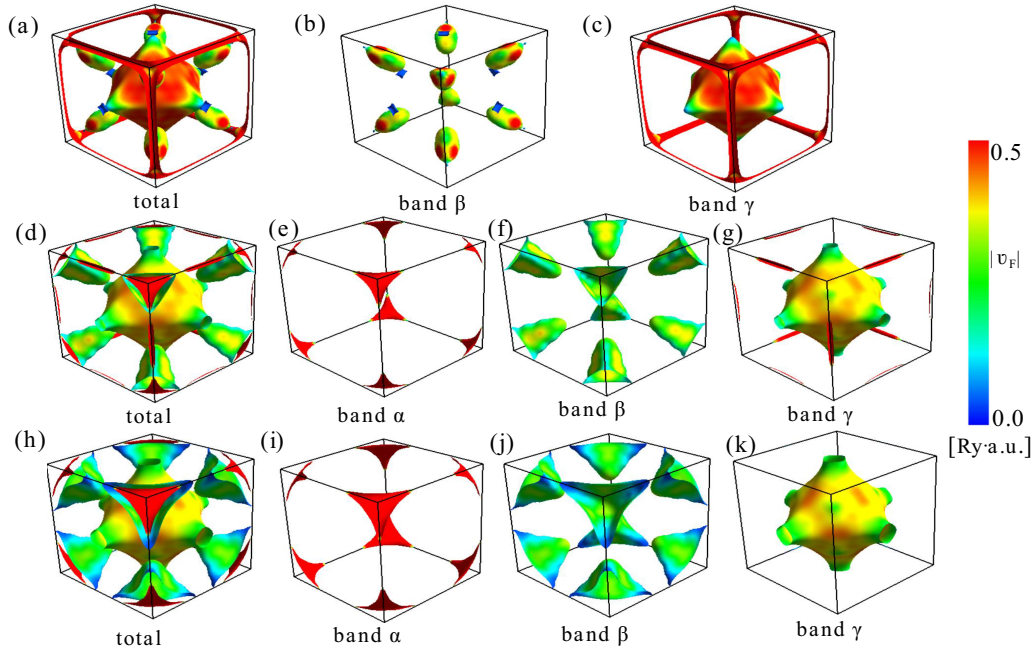


FIG. 4. Total Fermi surfaces (a) and the Fermi surfaces projected on the bands β (b) and γ (c) crossing the Fermi level for MgCPd_3 . Total Fermi surfaces (d) and projected on the bands α (e), β (f), and γ (g) crossing the Fermi level for CaCPd_3 . (h), (i), (j), (k), the same as (d), (e), (f), (g) but for SrCPd_3 . The bands α , β , and γ are highlighted in Fig. 2.

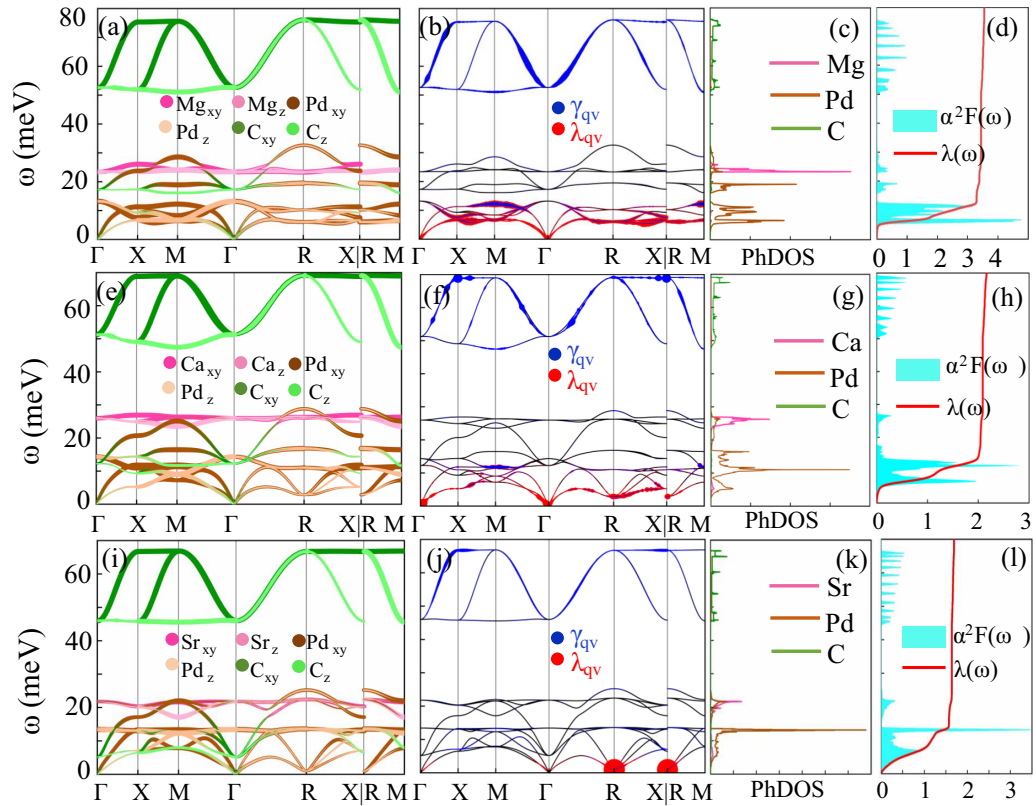


FIG. 5. Calculated (a) phonon dispersion weighted by the vibrational modes, (b) the phonon dispersion weighted by the magnitude of EPC λ_{qv} (red balls) and phonon linewidth γ_{qv} (red balls), (c) the total and atom-projected PhDOS, and (d) the Eliashberg spectral function and cumulative frequency-dependent EPC function λ for MgCPd_3 . [(e)–(h)] Same as (a)–(d) but for CaCPd_3 . [(i)–(l)] Same as (a)–(d) but for SrCPd_3 .

TABLE I. The calculated $N(E_F)$ (states/spin/eV/unit cell), the total EPC parameter λ , the logarithmic average phonon frequency ω_{\log} (K), the superconducting gap (meV), and the superconducting transition temperature T_c (K) of ACPd₃ ($A = \text{Mg, Ca, Sr}$) and MgCNi₃. The previous results of MgCNi₃ are also presented in the parentheses for comparison.

Compound	$N(E_F)$	λ	ω_{\log}	Δ	T_c
MgCPd ₃	1.80	3.50	99.14	2.89	19.05
CaCPd ₃	1.99	2.05	105.12	2.33	15.37
SrCPd ₃	2.44	1.67	81.66	1.55	10.25
MgCNi ₃	2.12 (2.40 [84])	0.85 (0.7 [26])	146.07	1.17 (0.77 [27])	7.71 (8 [26], 8.5 [84], 9.1 [52])

low frequency at 13 meV, accompanying with a sharp peak in Fig. 5(k). Interestingly, the acoustic branches dominated by the vibrations of Pd atoms at the high-symmetry point R show significant softening.

The phonon dispersion weighted by the magnitude of the phonon linewidth γ_{qv} and the EPC strength λ_{qv} are illustrated in Figs. 5(b), 5(f), and 5(j). It is clear that the high-frequency optical branches dominated by the vibration of C atoms have larger phonon linewidths γ_{qv} than the low-frequency branches (below 13 meV) contributed by Pd-atom vibrations for these three perovskites. γ_{qv} is proportional to inverse phonon lifetime. It is reasonable that the phonons with higher frequency contributed by the lighter atoms often have shorter lifetime (large linewidths) and are easier to be scattered. Specially, the low-energy phonon bands (below 13 meV) of MgCPd₃ have strong EPC strength λ_{qv} [shown in Fig. 5(b)], which can give the main contribution to the phonon-mediated superconductivity. The strong EPC λ_{qv} strength also appears in the low-energy phonon bands (below 13 meV) of CaCPd₃. And for SrCPd₃, the softened modes at the high-symmetry point R in the low-energy three acoustic branches are characterized by strong EPC λ_{qv} . In addition, the intermediate-frequency region (19–28 meV) dominated by the vibrations of alkaline-earth metal atoms scarcely contributes to both γ_{qv} and λ_{qv} .

The calculated Eliashberg electron-phonon spectral function $\alpha^2F(\omega)$, and the integrated strength of the EPC λ are plotted in Figs. 5(d), 5(h), and 5(l). As shown, the EPC λ below 13 meV reaches 93%, 98%, and 94% of the total EPCs for MgCPd₃, CaCPd₃, and SrCPd₃, respectively. Although the distributions of $\alpha^2F(\omega)$ are non-negligible at the high-frequency region (above 13 meV), their contribution to the EPC is limited. It is easily to understand such phenomena by Eq. (4). The total EPC strengths for MgCPd₃, CaCPd₃, and SrCPd₃ are calculated to be 3.50, 2.05, and 1.67, respectively. Thus this family of materials can be classified as strong superconductors under ambient conditions. Taking λ and $\alpha^2F(\omega)$ into Eq. (6), one can obtain the superconducting transition temperature T_c . The calculated T_c as well as superconducting parameters of λ , ω_{\log} , and superconducting gap Δ of ACPd₃ are listed in Table I. For these three perovskites, the obtained λ , Δ , and T_c have the same trend: decreasing with the increase in the atomic number. The simulated T_c for MgCPd₃, CaCPd₃, and SrCPd₃ are 19.05, 15.37, and 10.25 K, respectively, and positively correlated with the EPC constant λ , suggesting that these systems are phonon-mediated superconductors. Moreover, at static zero pressure, the intrinsic T_c

of MgCPd₃ (19.05 K) is comparable to that of the perovskite superconductor PthBe₃ (17.8 K) [52] and the iron-based superconductor LiFeAs (18 K) [17].

In addition, using the same theoretical simulation parameters, we also check the superconducting parameters λ , ω_{\log} as well as T_c of MgCNi₃. The calculated results are also listed in Table I, which are in accordance with the previous reported theoretical and experimental data [26,27,52,84], demonstrating the reliability of the present theoretical method. Thus the calculated superconducting properties of ACPd₃ ($A = \text{Mg, Ca, Sr}$) are reasonable when the SOC is omitted. In addition, we examine the influence of the Coulomb potential μ^* on the superconductivity critical temperature T_c . As shown in Fig. S9 [68], the T_c values of all three materials decrease with increasing μ^* .

D. Tunable superconductivity

Now, we will try to demonstrate the variation trend of superconductivity in ACPd₃ ($A = \text{Mg, Ca, Sr}$). Let's begin with MgCNi₃ and MgCPd₃, Fig. S1(a) [68] reveals MgCNi₃ and MgCPd₃ have similar electronic band structures around the Fermi level, especially the VHS and FB. As a result, the hole pocket (band β) and electron pocket (band γ) with comparable size emerge in the Fermi surface for MgCNi₃ [85] and MgCPd₃, respectively (see Figs. 4(a) and S8 [68]). Although MgCPd₃ has a slightly smaller $N(E_F)$ than MgCNi₃, the T_c of MgCPd₃ is almost twice as much as that of MgCNi₃, which might attribute to the much stronger EPC of MgCPd₃ than that of MgCNi₃ (Table I). The stronger EPC of MgCPd₃ might ascribe to the much larger SOC strength of Pd than Ni. Actually, the SOC strength is approximately proportional to Z^4 [86] (where Z is the atomic number; $Z_{\text{Pd}} = 46$ for Pd and $Z_{\text{Ni}} = 28$ for Ni). The ratio $(Z_{\text{Pd}}/Z_{\text{Ni}})^4 \approx 7.3$ and consequently the SOC strength will increase dramatically when Ni is substituted by Pd. The phenomenon that the stronger SOC would lead to a larger EPC and thus give rise to a higher T_c has also been reported in the Pd-substituted perovskite superconductor SrPPT₃ [86] and Ta-substituted kagome superconductor CsV₃Sb₅ [87].

Then, we would try to understand the decreasing tendency of T_c from MgCPd₃ to SrCPd₃. Although $N(E_F)$ increases gradually from MgCPd₃ to SrCPd₃, the EPC strength suffers a downtrend accompanied by the decline of T_c from MgCPd₃ to SrCPd₃ (Table I). This point might attribute to the decreasing electron correlation strength from MgCPd₃ to SrCPd₃. As clearly shown in the left panels of Fig. 2, the

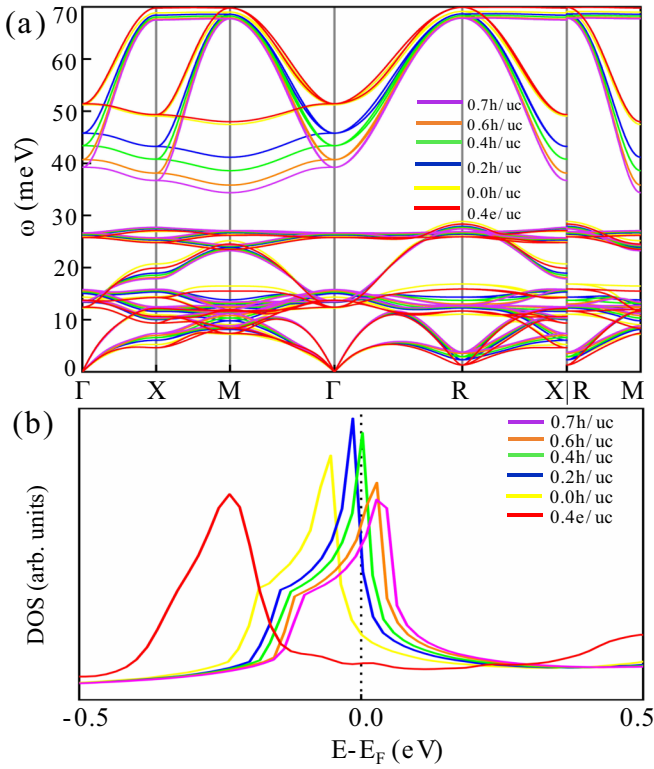


FIG. 6. The phonon dispersion curves (a) and total density of states (b) with different doping concentrations for CaCPd₃, where the SOC effect is absent.

FB just locates at the Fermi level for MgCPd₃ while the FB is below the Fermi level for CaCPd₃ and SrCPd₃. Besides, the band β around the M point (indicated by the dashed rectangles) is more dispersive for SrCPd₃ than MgCPd₃ and CaCPd₃. Moreover, the Fermi velocity $|v_F|$ projected to the (110) plane indicates the electrons are more localized for MgCPd₃ than CaCPd₃ and SrCPd₃ (Fig. S7 [68]). These phenomena suggest the electron correlation strength of the Fermi surface is MgCPd₃ > CaCPd₃ > SrCPd₃. As a result, the stronger electron correlation would bring in a larger EPC parameter and thus achieve a higher T_c for MgCPd₃. This is consistent with the previous reports where the stronger correlation is beneficial to superconductivity [88,89]. To further verify this viewpoint, electron and hole doping are introduced for CaCPd₃, and the corresponding superconducting properties are acquired.

As displayed in Fig. 6(a), CaCPd₃ maintains dynamically stable for the given doping concentrations. In particular, when the doping concentration varies from 0.4 electrons/unit cell (0.4 e/uc) to 0.7 holes/unit cell (0.7 h/uc), the VHS and FB move towards the Fermi level (Fig. S10 [68]) and the FSs are modified in a moderate degree (Fig. S11 [68]). Meanwhile, the DOS peak first shifts towards and then crosses over the Fermi level [Fig. 6(b)], where $N(E_F)$ first increases until the VHS lies at the Fermi level (0.4 h/uc) and then decrease with the increasing hole doping (Table II). As for the 0.4 electrons doping, the VHS and FB are away from the Fermi level (Fig. S10(a) [68]) and the $N(E_F)$ is much smaller than others,

TABLE II. The superconducting properties including the $N(E_F)$ (states/spin/eV/unit cell), the total EPC parameter λ , the logarithmic average phonon frequency ω_{\log} (K) and the superconducting transition temperature T_c (K) under various doping concentrations of CaCPd₃.

Doping	$N(E_F)$	λ	ω_{\log}	T_c
0.4 e/uc	0.95	1.68	69.98	8.83
0.0 h/uc	1.99	2.05	105.12	15.37
0.2 h/uc	3.99	2.16	106.65	16.13
0.4 h/uc	6.61	2.23	107.77	16.62
0.6 h/uc	4.51	2.51	109.36	18.05
0.7 h/uc	3.93	2.61	109.38	18.41

resulting in a much lower T_c (Table II). With the increasing hole doping concentration, the band along $X-M$ path becomes more and more flat (Fig. S10 [68]), which implies the electron correlation strength grows slightly. As a consequence, the T_c rises gradually with the increasing EPC strength (Table II). Now, we can conclude that the enhanced electron correlation and the large $N(E_F)$ stemming from the VHS and FB near the Fermi level may be reasonable for the enhancement of the electron-phonon coupling, which leads to the increase of T_c .

IV. CONCLUSION

In summary, based on first-principles calculations, we present a systematic study on the topological properties and superconductivity of the cubic perovskites ACPd₃ ($A = \text{Mg, Ca, Sr}$). Their structural stability is firstly verified from thermodynamic, mechanical and dynamic aspects. The Dirac points with nontrivial topological surface states are confirmed by the calculations of irreducible representations. The phonon-mediated superconductivity is solved based on the Eliashberg equation. The calculated superconducting critical temperatures of ACPd₃ ($A = \text{Mg, Ca, Sr}$) are 19.05, 15.37, and 10.25 K, which are much larger than that of MgCNi₃ ($T_c = 7.71$ K). This can be attributed to the much stronger electron-phonon coupling that stems from the larger SOC strength of Pd than Ni. The enhancement of EPC from SrCPd₃ to MgCPd₃ is closely related to the enhanced electron correlation deriving from the VHS and FB near the Fermi level. The coexistence of VHS, flat band, Dirac point, and superconductivity suggests that these three perovskites are promising candidates for exploring the interaction between multiple states.

ACKNOWLEDGMENTS

This work was supported by the National Natural Science Foundation of China (Grants No. 11904297, No. 11504301 and No. 11704315), the Chongqing Talent Plan for Young Top Notch Talents, China (Grant No. CQYC202005007) and the Fundamental Research Funds for the Central Universities (Grant No. SWU-KT22049).

- [1] J.-X. Yin, B. Lian, and M. Z. Hasan, *Nature (London)* **612**, 647 (2022).
- [2] X. Teng, L. Chen, F. Ye, E. Rosenberg, Z. Liu, J.-X. Yin, Y.-X. Jiang, J. S. Oh, M. Z. Hasan, K. J. Neubauer, B. Gao, Y. Xie, M. Hashimoto, D. Lu, C. Jozwiak, A. Bostwick, E. Rotenberg, R. J. Birgeneau, J.-H. Chu, M. Yi *et al.*, *Nature (London)* **609**, 490 (2022).
- [3] J.-X. Yin, S. S. Zhang, G. Chang, Q. Wang, S. S. Tsirkin, Z. Guguchia, B. Lian, H. Zhou, K. Jiang, I. Belopolski, N. Shumiya, D. Multer, M. Litskevich, T. A. Cochran, H. Lin, Z. Wang, T. Neupert, S. Jia, H. Lei, and M. Z. Hasan, *Nat. Phys.* **15**, 443 (2019).
- [4] M.-X. Wu, Y.-H. Wei, D.-S. Ma, P. Wang, N. Gao, S.-Y. Wu, and M.-Q. Kuang, *Phys. Rev. B* **108**, 174430 (2023).
- [5] S. Cho, H. Ma, W. Xia, Y. Yang, Z. Liu, Z. Huang, Z. Jiang, X. Lu, J. Liu, Z. Liu, J. Li, J. Wang, Y. Liu, J. Jia, Y. Guo, J. Liu, and D. Shen, *Phys. Rev. Lett.* **127**, 236401 (2021).
- [6] K. Jiang, T. Wu, J.-X. Yin, Z. Wang, M. Z. Hasan, S. D. Wilson, X. Chen, and J. Hu, *Natl. Sci. Rev.* **10**, nwc199 (2023).
- [7] X.-W. Yi, Z.-W. Liao, J.-Y. You, B. Gu, and G. Su, *Research* **6**, 0238 (2023).
- [8] J.-G. Si, L.-T. Shi, P.-F. Liu, P. Zhang, and B.-T. Wang, *Phys. Rev. B* **106**, 214527 (2022).
- [9] Y. Cao, V. Fatemi, A. Demir, S. Fang, S. L. Tomarken, J. Y. Luo, J. D. Sanchez-Yamagishi, K. Watanabe, T. Taniguchi, E. Kaxiras, R. C. Ashoori, and P. Jarillo-Herrero, *Nature (London)* **556**, 80 (2018).
- [10] Y. Cao, V. Fatemi, S. Fang, K. Watanabe, T. Taniguchi, E. Kaxiras, and P. Jarillo-Herrero, *Nature (London)* **556**, 43 (2018).
- [11] C.-C. Liu, L.-D. Zhang, W.-Q. Chen, and F. Yang, *Phys. Rev. Lett.* **121**, 217001 (2018).
- [12] A. Kerelsky, L. J. McGilly, D. M. Kennes, L. Xian, M. Yankowitz, S. Chen, K. Watanabe, T. Taniguchi, J. Hone, C. Dean, A. Rubio, and A. N. Pasupathy, *Nature (London)* **572**, 95 (2019).
- [13] R. S. Markiewicz, B. Singh, C. Lane, and A. Bansil, *Commun. Phys.* **6**, 292 (2023).
- [14] M. Horio, K. Hauser, Y. Sassa, Z. Mingazheva, D. Sutter, K. Kramer, A. Cook, E. Nocerino, O. K. Forslund, O. Tjernberg, M. Kobayashi, A. Chikina, N. B. M. Schröter, J. A. Krieger, T. Schmitt, V. N. Strocov, S. Pyon, T. Takayama, H. Takagi, O. J. Lipscombe *et al.*, *Phys. Rev. Lett.* **121**, 077004 (2018).
- [15] C. C. Tsuei, D. M. Newns, C. C. Chi, and P. C. Pattnaik, *Phys. Rev. Lett.* **65**, 2724 (1990).
- [16] K. Gofron, J. C. Campuzano, A. A. Abrikosov, M. Lindroos, A. Bansil, H. Ding, D. Koelling, and B. Dabrowski, *Phys. Rev. Lett.* **73**, 3302 (1994).
- [17] S. V. Borisenko, V. B. Zabolotnyy, D. V. Evtushinsky, T. K. Kim, I. V. Morozov, A. N. Yaresko, A. A. Kordyuk, G. Behr, A. Vasiliev, R. Follath, and B. Büchner, *Phys. Rev. Lett.* **105**, 067002 (2010).
- [18] J. Baglo, J. Chen, K. Murphy, R. Leenen, A. McCollam, M. L. Sutherland, and F. M. Grosche, *Phys. Rev. Lett.* **129**, 046402 (2022).
- [19] K. Nakayama, Y. Miyata, G. N. Phan, T. Sato, Y. Tanabe, T. Urata, K. Tanigaki, and T. Takahashi, *Phys. Rev. Lett.* **113**, 237001 (2014).
- [20] Z. Jiang, Z. Liu, H. Ma, W. Xia, Z. Liu, J. Liu, S. Cho, Y. Yang, J. Ding, J. Liu, Z. Huang, Y. Qiao, J. Shen, W. Jing, X. Liu, J. Liu, Y. Guo, and D. Shen, *Nat. Commun.* **14**, 4892 (2023).
- [21] J. G. Bednorz and K. A. Müller, *Rev. Mod. Phys.* **60**, 585 (1988).
- [22] A. H. C. Neto, G. Castilla, and B. A. Jones, *Phys. Rev. Lett.* **81**, 3531 (1998).
- [23] S.-S. Lee, *Annu. Rev. Condens. Matter Phys.* **9**, 227 (2018).
- [24] P. G. Khalifah, K. D. Nelson, R. Jin, Z. Mao, Y. Liu, Q. Huang, Q. Huang, X. P. A. Gao, A. P. Ramirez, A. P. Ramirez, and R. J. Cava, *Nature (London)* **411**, 669 (2001).
- [25] P. Tong, Y. P. Sun, X. B. Zhu, and W. H. Song, *Phys. Rev. B* **73**, 245106 (2006).
- [26] T. He, Q. Huang, A. P. Ramirez, Y. Wang, K. A. Regan, N. Rogado, M. A. Hayward, M. K. Haas, J. S. Slusky, K. Inumara, H. W. Zandbergen, N. P. Ong, and R. J. Cava, *Nature (London)* **411**, 54 (2001).
- [27] J. Kačmarčík, Z. Pribulová, P. Szabó, P. Samuely, C. Marcenat, T. Klein, D.-J. Jang, H.-G. Lee, H.-S. Lee, and S. Lee, *J. Phys. Chem. Solids* **69**, 3011 (2008).
- [28] J.-Y. Lin, P. L. Ho, H. L. Huang, P. H. Lin, Y.-L. Zhang, R.-C. Yu, C.-Q. Jin, and H. D. Yang, *Phys. Rev. B* **67**, 052501 (2003).
- [29] L. Shan, Z. Y. Liu, Z. A. Ren, G. C. Che, and H. H. Wen, *Phys. Rev. B* **71**, 144516 (2005).
- [30] X. F. Lu, L. Shan, Z. Wang, H. Gao, Z. A. Ren, G. C. Che, and H. H. Wen, *Phys. Rev. B* **71**, 174511 (2005).
- [31] R. T. Gordon, N. D. Zhigadlo, S. Weyeneth, S. Katrych, and R. Prozorov, *Phys. Rev. B* **87**, 094520 (2013).
- [32] L. Shan, H. J. Tao, H. Gao, Z. Z. Li, Z. A. Ren, G. C. Che, and H. H. Wen, *Phys. Rev. B* **68**, 144510 (2003).
- [33] P. Diener, P. Rodière, T. Klein, C. Marcenat, J. Kacmarcik, Z. Pribulova, D. J. Jang, H. S. Lee, H. G. Lee, and S. I. Lee, *Phys. Rev. B* **79**, 220508(R) (2009).
- [34] R. Prozorov, A. Snezhko, T. He, and R. J. Cava, *Phys. Rev. B* **68**, 180502(R) (2003).
- [35] Z. Q. Mao, M. M. Rosario, K. D. Nelson, K. Wu, I. G. Deac, P. Schiffer, Y. Liu, T. He, K. A. Regan, and R. J. Cava, *Phys. Rev. B* **67**, 094502 (2003).
- [36] Z. Pribulová, J. Kačmarčík, C. Marcenat, P. Szabó, T. Klein, A. Demuer, P. Rodiere, D. J. Jang, H. S. Lee, H. G. Lee, S.-I. Lee, and P. Samuely, *Phys. Rev. B* **83**, 104511 (2011).
- [37] D. P. Young, M. Moldovan, and P. W. Adams, *Phys. Rev. B* **70**, 064508 (2004).
- [38] R. M. Welsh, *Nature (London)* **411**, 541 (2001).
- [39] A. Dong, G. Che, W. Huang, S. Jia, H. Chen, and Z. Zhao, *Physica C: Superconductivity* **422**, 65 (2005).
- [40] P. Tong, Y. P. Sun, X. B. Zhu, and W. H. Song, *Phys. Rev. B* **74**, 224416 (2006).
- [41] H. Takei, N. Kobayashi, H. Yamauchi, T. Shishido, and T. Fukase, *J. Less-Common Met.* **125**, 233 (1986).
- [42] B. Wiendlocha, J. Tobola, and S. Kaprzyk, *Phys. Rev. B* **73**, 134522 (2006).
- [43] J.-T. Zhao, Z.-C. Dong, J. Vaughey, J. E. Ostenson, and J. D. Corbett, *J. Alloys Compd.* **230**, 1 (1995).
- [44] M. Uehara, A. Uehara, K. Kozawa, and Y. Kimishima, *J. Phys. Soc. Jpn.* **78**, 033702 (2009).
- [45] B. He, C. Dong, L. Yang, X. Chen, L. Ge, L. Mu, and Y. Shi, *Supercond. Sci. Technol.* **26**, 125015 (2013).
- [46] M. Uehara, A. Uehara, K. Kozawa, T. Yamazaki, and Y. Kimishima, *Phys. C* **470**, S688 (2010).

- [47] H. M. Tütüncü and G. P. Srivastava, *J. Appl. Phys.* **112**, 093914 (2012).
- [48] H. M. Tütüncü and G. P. Srivastava, *J. Appl. Phys.* **114**, 053905 (2013).
- [49] M. Oudah, A. Ikeda, J. N. Hausmann, S. Yonezawa, T. Fukumoto, S. Kobayashi, M. Sato, and Y. Maeno, *Nat. Commun.* **7**, 13617 (2016).
- [50] E. Haque and M. A. Hossain, *J. Alloys Compd.* **730**, 279 (2018).
- [51] S. Ram and V. Kanchana, *Solid State Commun.* **181**, 54 (2014).
- [52] N. Hoffmann, T. F. T. Cerqueira, J. Schmidt, and M. A. L. Marques, *npj Comput. Mater.* **8**, 150 (2022).
- [53] P. Giannozzi, S. Baroni, N. Bonini, M. Calandra, R. Car, C. Cavazzoni, D. Ceresoli, G. L. Chiarotti, M. Cococcioni, I. Dabo *et al.*, *J. Phys.: Condens. Matter* **21**, 395502 (2009).
- [54] J. P. Perdew, K. Burke, and M. Ernzerhof, *Phys. Rev. Lett.* **77**, 3865 (1996).
- [55] P. E. Blöchl, *Phys. Rev. B* **50**, 17953 (1994).
- [56] S. Baroni, S. de Gironcoli, A. D. Corso, and P. Giannozzi, *Rev. Mod. Phys.* **73**, 515 (2001).
- [57] M. J. Verstraete, M. Torrent, F. Jollet, G. Zérah, and X. Gonze, *Phys. Rev. B* **78**, 045119 (2008).
- [58] M. Kawamura, *Comput. Phys. Commun.* **239**, 197 (2019).
- [59] M. P. L. Sancho, J. M. L. Sancho, J. M. L. Sancho, and J. Rubio, *J. Phys. F: Met. Phys.* **15**, 851 (1985).
- [60] Q. Wu, S. Zhang, H.-F. Song, M. Troyer, and A. A. Soluyanov, *Comput. Phys. Commun.* **224**, 405 (2018).
- [61] I. Souza, N. Marzari, and D. Vanderbilt, *Phys. Rev. B* **65**, 035109 (2001).
- [62] N. Marzari, A. A. Mostofi, J. R. Yates, I. Souza, and D. Vanderbilt, *Rev. Mod. Phys.* **84**, 1419 (2012).
- [63] G. Kresse and J. Furthmüller, *Phys. Rev. B* **54**, 11169 (1996).
- [64] P. B. Allen and R. C. Dynes, *Phys. Rev. B* **12**, 905 (1975).
- [65] B. Mühlischlegel, *Zeitschrift für Physik* **155**, 313 (1959).
- [66] U. E. Musanke and W. Jeitschko, *Zeitschrift für Naturforschung B* **46**, 1177 (1991).
- [67] J. T. Haraldsen and R. S. Fishman, *J. Phys.: Condens. Matter* **21**, 216001 (2009).
- [68] See Supplemental Material at <http://link.aps.org/supplemental/10.1103/PhysRevB.110.064519> for the following: Projected band structures of different orbits; Irreducible representations and topological surface states of the crossing points; The (110) plane views of projections of the atomic orbitals to the electronic states on the Fermi surfaces; The (110) plane views of Fermi velocity on the Fermi surfaces; The 3D views of Fermi velocity of MgCNi₃; Superconducting temperature T_c of ACPd₃ ($A = \text{Mg, Ca, Sr}$) as a function of the Coulomb potential; The electronic band structures of CaCPd₃ with different electron and hole doping concentrations without SOC; The 3D views of Fermi velocity with different electron and hole doping concentrations; The crystal parameters, elastic constants and formation energy of ACPd₃ ($A = \text{Mg, Ca, Sr}$).
- [69] M. E. Barber, A. S. Gibbs, Y. Maeno, A. P. Mackenzie, and C. W. Hicks, *Phys. Rev. Lett.* **120**, 076602 (2018).
- [70] R. Markiewicz, *J. Phys. Chem. Solids* **58**, 1179 (1997).
- [71] R. Mori, P. B. Marshall, K. Ahadi, J. D. Denlinger, S. Stemmer, and A. Lanzara, *Nat. Commun.* **10**, 5534 (2019).
- [72] Y. Wang, H. Wu, G. T. McCandless, J. Y. Chan, and M. N. Ali, *Nat. Rev. Phys.* **5**, 635 (2023).
- [73] M. Iraola, J. L. Mañes, B. Bradlyn, M. K. Horton, T. Neupert, M. G. Vergniory, and S. S. Tsirkin, *Comput. Phys. Commun.* **272**, 108226 (2022).
- [74] Z.-M. Yu, Z. Zhang, G.-B. Liu, W. Wu, X.-P. Li, R.-W. Zhang, S. A. Yang, and Y. Yao, *Sci. Bull.* **67**, 375 (2022).
- [75] Z. Luo, X. Hu, M. Wang, W. Wú, and D.-X. Yao, *Phys. Rev. Lett.* **131**, 126001 (2023).
- [76] S. E. Sebastian, N. Harrison, P. A. Goddard, M. M. Altarawneh, C. H. Mielke, R. Liang, D. A. Bonn, W. N. Hardy, O. K. Andersen, and G. G. Lonzarich, *Phys. Rev. B* **81**, 214524 (2010).
- [77] Y. Zhang, L.-F. Lin, A. Moreo, and E. Dagotto, *Phys. Rev. B* **108**, L180510 (2023).
- [78] J. Ishizuka, S. Sumita, A. Daido, and Y. Yanase, *Phys. Rev. Lett.* **123**, 217001 (2019).
- [79] D. Steffensen, A. Kreisel, P. J. Hirschfeld, and B. M. Andersen, *Phys. Rev. B* **103**, 054505 (2021).
- [80] C.-H. Lin, T. Berlijn, L. Wang, C.-C. Lee, W.-G. Yin, and W. Ku, *Phys. Rev. Lett.* **107**, 257001 (2011).
- [81] W. Xia, X. Shi, Y. Zhang, H. Su, Q. Wang, L. Ding, L. Chen, X. Wang, Z. Zou, N. Yu, L. Pi, Y. Hao, B. Li, Z. Zhu, W. Zhao, X. Kou, and Y. Guo, *Phys. Rev. B* **101**, 155117 (2020).
- [82] W. Huang, H. Lin, C. Zheng, Y. Yin, X. Chen, and S.-H. Ji, *Phys. Rev. B* **103**, 094502 (2021).
- [83] C. Broyles, Z. Rehfuss, H. Siddiquee, J. A. Zhu, K. Zheng, M. Nikolo, D. Graf, J. Singleton, and S. Ran, *Phys. Rev. Lett.* **131**, 036501 (2023).
- [84] H. Rosner, R. Weht, M. D. Johannes, W. E. Pickett, and E. Tosatti, *Phys. Rev. Lett.* **88**, 027001 (2001).
- [85] D. J. Singh and I. I. Mazin, *Phys. Rev. B* **64**, 140507(R) (2001).
- [86] K. Hu, B. Gao, Q. Ji, Y. Ma, W. Li, X. Xu, H. Zhang, G. Mu, F. Huang, C. Cai, X. Xie, and M. Jiang, *Phys. Rev. B* **93**, 214510 (2016).
- [87] Y. Luo, Y. Han, J. Liu, H. Chen, Z. Huang, L. Huai, H. Li, B. Wang, J. Shen, S. Ding, Z. Li, S. Peng, Z. Wei, Y. Miao, X. Sun, Z. Ou, Z. Xiang, M. Hashimoto, D. Lu, Y. Yao *et al.*, *Nat. Commun.* **14**, 3819 (2023).
- [88] L. Balents, C. R. Dean, D. K. Efetov, and A. F. Young, *Nat. Phys.* **16**, 725 (2020).
- [89] D. M. Kennes, J. Lischner, and C. Karrasch, *Phys. Rev. B* **98**, 241407(R) (2018).